Cellulose (2015) 22:1517–1539
DOI 10.1007/s10570-015-0610-6

ORIGINAL PAPER

3D analysis of paper microstructures at the scale of fibres and bonds

Cyril Marulier · Pierre J. J. Dumont · Laurent Orgéas · Sabine Rolland du Roscoat · Denis Caillerie

Received: 8 October 2014 / Accepted: 19 March 2015 / Published online: 31 March 2015

Abstract The evolution of paper microstructure parameters, such as porosity and fibre orientation, as a function of papermaking conditions is most often studied at a macroscopic scale. However, modelling the physical and mechanical properties of papers using upscaling approaches requires understanding the deformation micro-mechanisms that are induced by papermaking operations within the structure of paper fibrous networks for individual fibres and fibre-to-fibre bonds. We addressed this issue by analysing three-dimensional images of model papers. These images were obtained using X-ray microtomography. The model papers were fabricated by varying forming, pressing, and drying conditions. For each image, this analysis enabled an unprecedented large set of geometrical parameters to be measured for individual fibres (centreline, shape and inclination of the fibre cross sections) and fibre-to-fibre bonds (inter-bond distance, number of bonds per unit length of fibre, bond surface area) within the fibrous networks. The evolution of the as-obtained microstructure parameters was analysed as a function of papermaking conditions. All results were in accordance with the data available in the literature. A key result was obtained for the evolution of the number of fibre-to-fibre contacts per fibre as a function of the network density. A representative number of contacts was obtained using relatively small imaged volumes. These volumes must only contain enough fibre segments the cumulated length of which is of the same order as the mean fibre length. These results were also used to validate microstructure models for the prediction of the number of fibre-to-fibre contacts within fibrous networks.

Keywords Lignocellulosic fibres · Fibre networks · X-ray microtomography · Microstructure descriptors · Fibres · Bonds

C. Marulier · P. J. J. Dumont (✉)
LGP2, Univ. Grenoble Alpes, 38000 Grenoble, France
e-mail: pierre.dumont@grenoble-inp.fr

C. Marulier · P. J. J. Dumont
LGP2, CNRS, 38000 Grenoble, France

C. Marulier · P. J. J. Dumont
LGP2, Agefpi, 38000 Grenoble, France

L. Orgéas · S. Rolland du Roscoat · D. Caillerie
3SR, Univ. Grenoble Alpes, 38000 Grenoble, France

L. Orgéas · S. Rolland du Roscoat · D. Caillerie
3SR, CNRS, 38000 Grenoble, France

S. Rolland du Roscoat
ID 19 Topography and Microtomography Group, ESRF, 38043 Grenoble Cedex, France

Introduction

Paper represents a distinctive class of fibrous materials and is one of the most widespread man-made fibrous materials. The main constituents of paper are lignocellulosic fibres (mainly wood pulp fibres) that form

its structural scaffold where mineral fillers and a small amount of other chemical products are added to obtain specific manufacturing or end-use properties. Paper can be considered to be a network of lignocellulosic fibres that are strongly linked together by chemical hydrogen bonding at their contacts. Various papers that exhibit a broad range of physical and mechanical properties can be fabricated using the same pulp. Thus, the choice of parameters for papermaking operations, such as fibre refining, forming, pressing, and drying, is crucial because all these operations induce drastic microstructural changes in the paper fibrous networks (Sampson 2009a; Alava and Niskanen 2006).

Relevant and accurate descriptions of paper microstructures (Bloch and Rolland du Roscoat 2009) must be obtained for the upscaling modelling approaches of the physical and mechanical properties of this material. More generally, the effects of the modifications induced by papermaking operations on the properties of paper must be understood at the microscopic scale, i.e., at the scale of fibres and bonds or contacts. However, it is difficult to experimentally determine microstructural descriptors for the morphology of fibres and bonds. Recent studies have focused on the analysis of fibre–fibre bonds that were individually prepared (Thomson et al. 2007, 2008a, b; Torgnysdotter et al. 2007; Kappel et al. 2009, 2010a, b). If these studies delivered very interesting results on the geometry of the fibre-to-fibre bond areas, the preparation conditions were rather far from papermaking conditions. In contrast, X-ray microtomography is unique as this technique can deliver three-dimensional images of fibres and fibre-to-fibre bonds inside fibrous networks that were obtained using various papermaking conditions (Rolland du Roscoat et al. 2007). Above their spatial resolution, X-ray microtomography images potentially contain a huge amount of geometrical and topological information about fibres and fibre-to-fibre bonds within paper fibrous networks. To date the exploitation of three-dimensional images has remained limited because of the current lack of automatic image analysis techniques to extract relevant information: see the review of automatic image analysis techniques reported by Viguié et al. (2013). However, in a preliminary study (Marulier et al. 2012), we demonstrated that a large set of microstructural descriptors for individual fibres and bonds can be obtained within the fibrous networks from X-ray microtomography images by using a "hand-made" and consequently time-consuming but efficient analysis.

Fig. 1 **a** Length and **b** width distributions of the maritime pine pulp fibres measured in wet conditions after the screening operation. *Top views* of **c** an in-plane isotropic model paper (σ_0 = 0.51 MPa, constrained drying) and **d** an in-plane orientated model paper (σ_0 = 0.42 MPa, constrained drying), and **e**, **f** corresponding fibre orientation distribution functions

In this study, we investigated the effects of papermaking conditions on the geometry of fibres and fibre-to-fibre bonds. For that purpose, model papers made up of unrefined softwood fibres were fabricated by varying forming (in-plane fibre orientation), pressing, and drying conditions. The influence of papermaking conditions on several microstructural descriptors for the fibres and the fibre-to-fibre bonds was measured using X-ray microtomography images. Statistical distribution functions were proposed for these descriptors. Besides, the influence of papermaking conditions on fibre-to-fibre bonds was investigated because this problem constitutes a major objective of microstructural analyses of paper fibrous networks (Bloch and Rolland du Roscoat 2009). For instance, good description of fibre bonds is a key input for the understanding of the mechanical performance of fibrous networks. Therefore, experimental measurements of the number of fibre-to-fibre bonds were compared to the theoretical predictions of both Sampson's model for in-plane isotropic fibrous networks (Sampson 2004; Eichhorn and Sampson 2005; Batchelor et al. 2006) and the so-called tube model (Toll 1993; Orgéas et al. 2012; Guiraud et al. 2012) adapted for networks of fibres that exhibit elliptical cross sections and planar fibre orientation (Guiraud et al. 2012). The description of fibre-to-fibre bonds also requires estimating the area of contacts and more generally the relative bonded area (RBA), i.e., the fraction of fibre surface that is in contact with other fibres within the fibrous networks (Ingmanson and Thode 1959). Using acquired data, both parameters were estimated.

Materials and experimental methods

Pulp fibres and model papers

Model papers were fabricated using an unbeaten bleached and classified softwood pulp from maritime pine. Even if unbeaten pulp fibres are not classically used for papermaking, unbeaten and classified pulp fibres were chosen to limit the complexity of the studied fibrous

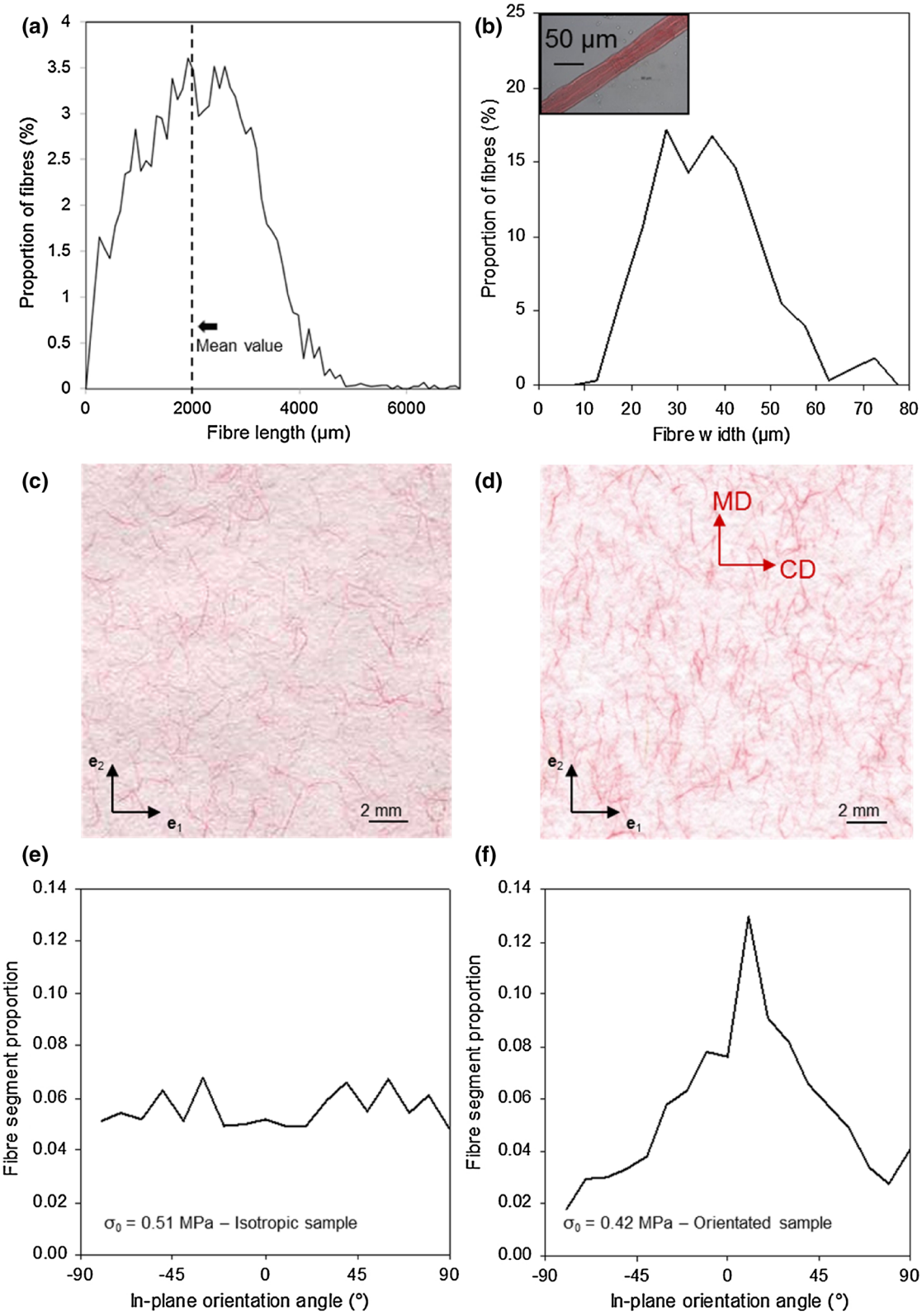
(a)
Proportion of fibres (%)
Mean value
Fibre length (μm)
(b)
50 μm
Proportion of fibres (%)
Fibre w idth (μm)
(c)
e2
e1
2 mm
(d)
MD
CD
e2
e1
2 mm
(e)
Fibre segment proportion
σ0 = 0.51 MPa – Isotropic sample
In-plane orientation angle (°)
(f)
Fibre segment proportion
σ0 = 0.42 MPa – Orientated sample
In-plane orientation angle (°)

networks. Figure 1a shows the length distribution of fibres: see Marulier et al. (2012) for the description of the Morfi apparatus (Techpap, Grenoble, France) that was used to make this measurement. This apparatus also enables the coarseness $\delta = 0.15$ mg m^{-1} to be measured. The fibre width distribution was measured in wet state using an optical microscopy technique (see Fig. 1b). Paper handsheets having a targeted basis weight $G = 40$ g m^{-2} were fabricated using a Rapid Köthen former (Karl Frank GMBH, Weinheim, Germany) or a dynamic handsheet former (Techpap, Grenoble, France) to confer an in-plane isotropic or an in-plane orientated structure to the fibrous networks, respectively. The obtained wet handsheets were then pressed between blotters for 3 min at a packing stress σ_0 that ranged from 0.10 to 0.91 MPa. The handsheets were finally dried using two methods: "free" drying and "in-plane constrained" drying. The first method consisted of drying handsheets in ambient air by placing them on a metal plate to prevent sticking. The handsheets could deform freely, which resulted in moderate in-plane and out-of-plane deformation phenomena: in-plane shrinkage of approximately −0.25 % was measured and few cockles were observed. The in-plane constrained drying method consisted of placing the handsheets in the dryer of the Rapid Köthen machine system for 6 min at 85 °C. After drying, the as-fabricated handsheets of model paper did not exhibit any in-plane shrinkage nor out-of-plane deformation. The constrained drying conditions are known to induce complex residual stress states in the fibrous networks (Uesaka et al. 1991).

The thickness t and the basis weight G of each handsheet were measured after storage in rooms where the temperature (T = 23 °C) and the relative humidity of the ambient air were controlled (50 % RH). These data were used to calculate the apparent density ρ_{app} of model papers. Their apparent porosity ϵ_{app} was also estimated from ρ_{app} and from the density of pure cellulose $\rho_{cellulose}$ of 1500 kg m^{-3} (Salmén and Fellers 1989), considering that fibres were only composed of cellulose:

$$\epsilon_{app} = 1 - \frac{\rho_{app}}{\rho_{cellulose}}. \quad (1)$$

The orientation distributions of fibres were measured by identifying the red dyed fibres appearing at the surface of the handsheets (see Fig. 1c, d) and by determining an in-plane orientation angle for each segment of all scanned fibres (Silvy 1980; Naito 2002). The orientation distribution functions became representative (stable) for approximately 1200 segments. Typical fibre orientation distributions are shown in Fig. 1e,f for isotropic papers and for in-plane orientated papers, respectively. For in-plane orientated papers, a preferential orientation of fibres was observed in the so-called machine direction "MD" (0°). Note that "CD" holds for cross direction (−90°/90°).

Basic mechanical properties

The mechanical properties of model papers were determined by using a commercial horizontal tensile testing device (Lorentzen and Wettre No. 162, tensile tester) installed in an air-conditioned room (temperature of 23 °C and relative humidity of 50 %). The Young's modulus E, the tensile strength T and the ultimate stress σ_u were estimated for each specimen (Niskanen and Krenlampi 1998).

Optical measurements and relative bonded area

The RBA of a fibrous network is defined by the following ratio: $\frac{A_T - A}{A_T}$, where A_T is the potential total area available for fibre bonding and A is the remaining unbonded fibre area after manufacturing.

An estimate of the RBA was made using the method developed by Ingmanson and Thode (1959) based on the measurement of the optical scattering coefficient ϑ_c of paper. In this method, ϑ_c is considered to be proportional to the total surface area $A_s \approx A$ available for light scattering. By determining the scattering coefficient ϑ_{c0} for a completely unbonded sheet of fibre area $A_{s0} \approx A_T$, an estimate for the RBA is obtained as follows:

$$RBA \approx \frac{A_{s0} - A_s}{A_{s0}} = \frac{\vartheta_{c0} - \vartheta_c}{\vartheta_{c0}}. \quad (2)$$

The optical scattering coefficient S_c can be obtained from light reflectances R_0 and R_∞ using the Kubelka and Munk theory [see for instance Leskelä (1998)]:

$$\vartheta_c = \frac{R_\infty}{G(1 - R_\infty^2)} \ln\left(\frac{1 - R_0 R_\infty}{R_\infty - R_0} R_\infty\right). \quad (3)$$

Practically, the measurements were made for all papers using a reflectance spectrophometer (Colour Touch 2, Technidyne, New Albany, IN, USA) at light

wavelength $\lambda = 457$ nm. Besides ϑ_{c0} was extrapolated from the evolution of ϑ_c as a function of the tensile strength T, as suggested by Ingmanson and Thode (1959).

Microstructure imaging by X-ray microtomography

X-ray microtomography experiments were performed at the European Synchrotron Radiation Facility (ESRF, ID19 beamline, Grenoble, France) to obtain 3D images of the microstructure of model papers (X-ray energy $= 17.6 \pm 0.9$ keV, CCD detector of 2048×2048 pixels, voxel size 0.7 µm × 0.7 µm × 0.7 µm, scanning time: <5 min). The dimensions of the scanned specimens that were cut in the handsheets were approximately 1.4 mm × 1.4 mm × t extracted from the produced sheets were achieved. Image treatments similar to those given in Marulier et al. (2012) were performed. Typical resulting images are shown in Fig. 2a, b. In the following sections, the measurements of microstructural descriptors were made using volumes of 140 µm × 140 µm × t, see Fig. 3a, or 200 µm × 100 µm × t.

Descriptors of fibres and fibre-to-fibre bonds

The operations of image analysis that were used to measure quantitative descriptors for the studied fibrous microstructures are briefly explained in this section and illustrated in Fig. 3. These operations were performed for nine scanned volumes representing different forming, pressing, and drying conditions.

Porosity

The porosity ϵ_X was calculated using the segmented 3D images as the ratio between the sum of the black voxels, i.e., the volume occupied by the pores, and the sum of all voxels, i.e., the volume of the imaged specimens. Compared to our previous study (Marulier et al. 2012), note that ϵ_X was calculated in the bulk of the paper microstructure (Rolland du Roscoat et al. 2007), i.e., the upper and lower "boundary layers" of paper were not taken into account. Consequently, the measured porosities are lower than those estimated in the aforementioned study (Marulier et al. 2012). The local bulk density $\rho_X = \rho_{cellulose}(1 - \epsilon_X)$ was also calculated.

Characterisation of the fibre centrelines

The fibre centrelines were determined by manually picking in the microtomography images the centres of mass of several cross sections of the fibres inside bonded zones (one picked point per fibre per bond zone) (Marulier et al. 2012; Guiraud et al. 2012). This procedure enabled the fibrous skeleton of each studied volume to be extracted (see Fig. 3b). The orientation of each segment of the centrelines was also characterised by both their angle in the sheet plane ψ_1 and their out-of-plane angle ψ_2 (see Fig. 3c):

$$\psi_1 = \tan^{-1}\left(\frac{\boldsymbol{AB}\cdot\boldsymbol{e}_2}{\boldsymbol{AB}\cdot\boldsymbol{e}_1}\right), \tag{4}$$

$$\psi_2 = \sin^{-1}\left(\frac{\boldsymbol{AB}\cdot\boldsymbol{e}_3}{\|\boldsymbol{AB}\|}\right). \tag{5}$$

Characterisation of the fibre cross section

The width L and the thicknesses l_1 and l_2 representing the principal dimensions of the fibre cross sections were measured (see Fig. 3d). The inclination angle θ between the major axis of the fibre cross section and the plane $(\boldsymbol{e}_1, \boldsymbol{e}_2)$ was also measured. To obtain

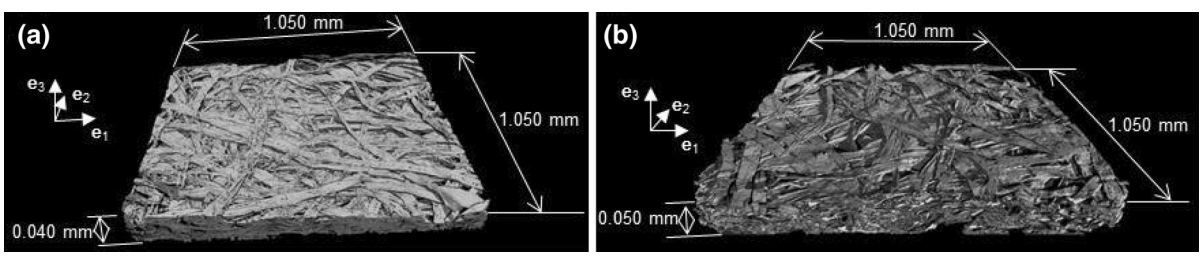

Fig. 2 3D images of **a** an in-plane isotropic paper ($\sigma_0 = 0.51$ MPa) and **b** an in-plane orientated paper ($\sigma_0 = 0.42$ MPa) that were obtained using X-ray microtomography. Both papers were dried under constraint

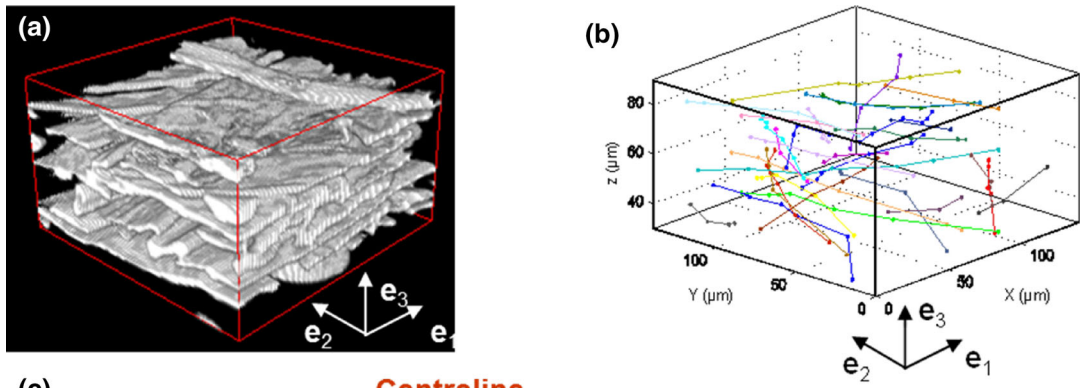
(a)
e3
e2
e1
(b)
z (μm)
80
60
40
100
50
0
Y (μm)
0
50
100
X (μm)
e3
e2
e1

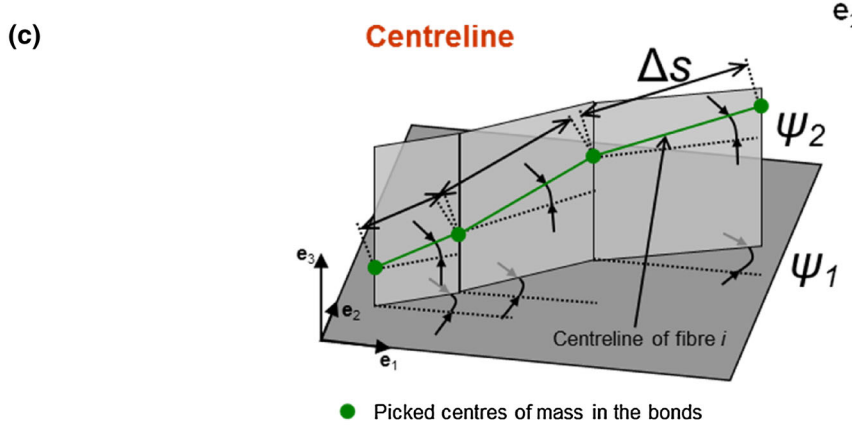
(c)
Centreline
Δs
ψ2
ψ1
e3
e2
e1
Centreline of fibre i
Picked centres of mass in the bonds

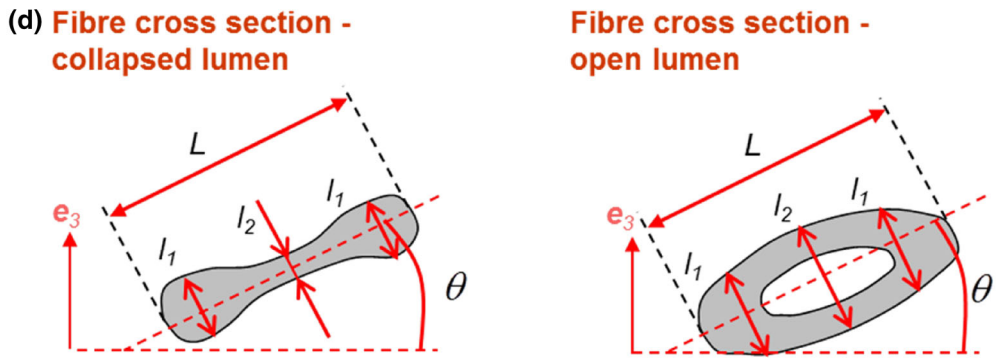
(d) Fibre cross section - collapsed lumen
L
l1
l2
l1
e3
θ
Fibre cross section - open lumen
L
l2
l1
l1
e3
θ

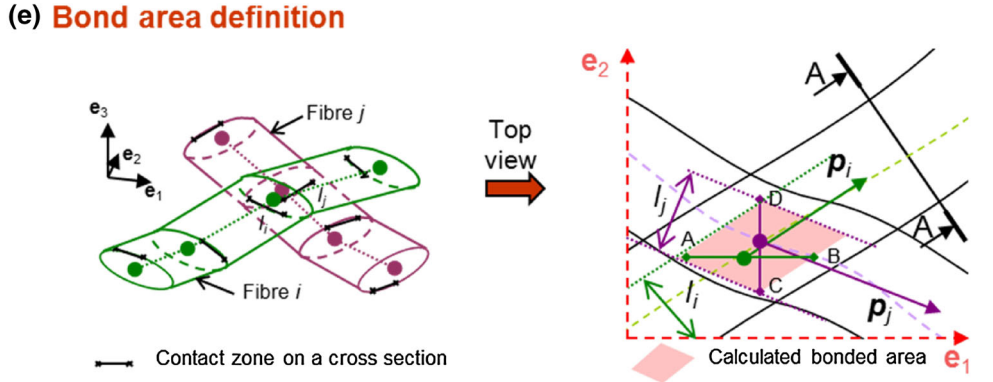
(e) Bond area definition
e3
e2
e1
Fibre j
lj
li
Fibre i
Contact zone on a cross section
Top view
e2
A
pi
lj
D
A
B
C
li
pj
A
Calculated bonded area
e1

◀**Fig. 3** **a** Volume of 140 μm × 140 μm × 90 μm extracted from the volume shown in Fig. 2. **b** Corresponding fibre skeleton. **c** Schematic view of a fibre centreline and its descriptors Ψ_1, Ψ_2 and Δs. **d** Schematic view of the fibre cross sections with a collapsed (*left*) or an open (*right*) lumen and their descriptors L, l_1, l_2 and θ. The principle of the method used to calculate the bond surface areas is illustrated in **e**. List of parameters: $(\boldsymbol{e}_1, \boldsymbol{e}_2, \boldsymbol{e}_3)$ frame of the microtomography image; Δs inter-bond distance; L fibre width; l_1 thickness close to the extremities of the fibre cross section; l_2 thickness in the middle of the fibre cross section, Ψ_1 angle in the sheet plane of the centreline segments relative to $\boldsymbol{e}_1$; Ψ_2 out-of-plane angle of the centreline segments relative to $(\boldsymbol{e}_1, \boldsymbol{e}_2)$; θ angle between the major axis of the fibre cross section and the sheet plane

statistical representative distributions, at least 120 measurements of each descriptor were taken for each scanned volume.

Characterisation of bonds

The curvilinear abscissae s_i of the centres of the bonds along the fibre centrelines were used to obtain the distance between the centre of two consecutive bonds k and l: $\Delta s_{kl} = s_k - s_l$.

The general aspect of bonds between two contacting fibres i and j is shown in Fig. 3e. The bond surface area S was roughly estimated as that of a parallelogram (right scheme in Fig. 3e):

$$S \approx \frac{l_i l_j}{\|\boldsymbol{p}_i \times \boldsymbol{p}_j\|}, \tag{6}$$

where l_i and l_j are the widths of the bond on the surface of fibre i and on the surface of fibre j, respectively. Practically, it was possible to assess the surface of about 80 bonds per specimen to build bond surface area distribution functions.

Characterisation of the bonding degree ratio

For each bond k identified along a fibre, the ratio l_k/L between the bond width l_k and the fibre width L was calculated. This measurement can be considered to be the bonding degree ratio between two contacting fibres: a ratio of one stands for a full contact and a lower ratio stands for a partial contact.

Microstructure and mechanical properties of the fibrous networks

Porosity

The apparent porosity ϵ_{app} of model papers decreased as the packing stress increased during wet pressing for all fibre orientations and drying conditions (see Fig. 4a, b), for in-plane isotropic and in-plane orientated papers, respectively. A sharp decrease in the apparent porosity was first observed. Then the porosity tended to stabilise as the packing stress increased. For in-plane isotropic and constrained dried papers, a 12 %-decrease in the apparent porosity was observed for a packing stress that ranged between 0.10 and 0.51 MPa, whereas this decrease was only of 4 % between 0.51 and 0.91 MPa. Note that the stabilisation at high packing stress of the consolidation of fibrous networks forming paper has been classically reported while the wet pressing conditions were increased (Luner et al. 1961; Alexander and Marton 1968). Similar trends were obtained for in-plane isotropic and orientated specimens. Likewise, drying conditions did not appear to have a large effect on the consolidation trends. However, constrained dried specimens exhibited a slight decrease in their porosity compared with freely dried specimens. This decrease can be attributed to the effect of the Rapid Köthen dryer in which the handsheets are placed between blotting papers and brought into contact with hot deformable rubber plates, which results in applying an extra packing stress onto the handsheets.

Similar results are shown for ϵ_X in the same graphs. The decrease in ϵ_X also corresponded to an increase in σ_0. However, ϵ_X was slightly different from ϵ_{app}. Differences are commonly encountered in using various methods for measuring paper porosity [see for instance the results reported by Niskanen and Rajatora (2002)]. In this study, this discrepancy between porosities could arise from the measurement method as well as from the size of the specimens that were used to determine ϵ_X and ϵ_{app}. The method for determining the apparent porosity ϵ_{app} could deform paper specimens as they were subjected to a slight compression stress (100 kPa) over a surface of 2 cm^2,

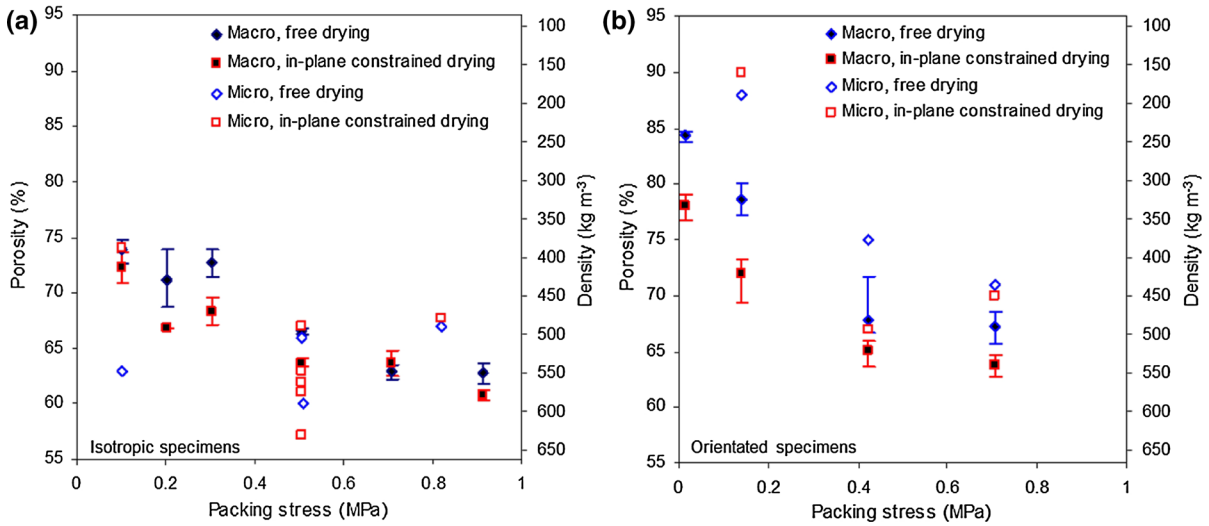

Fig. 4 **a**, **b** Porosities ϵ_{app} and ϵ_X and corresponding densities ρ_{app} as a function of the packing stress σ_0 for **a** the in-plane isotropic papers and **b** the in-plane orientated papers. The data of the apparent porosity ρ_{app} were averaged over five tests for each paper. The minimum and maximum values were used to show the scattering of the measurements

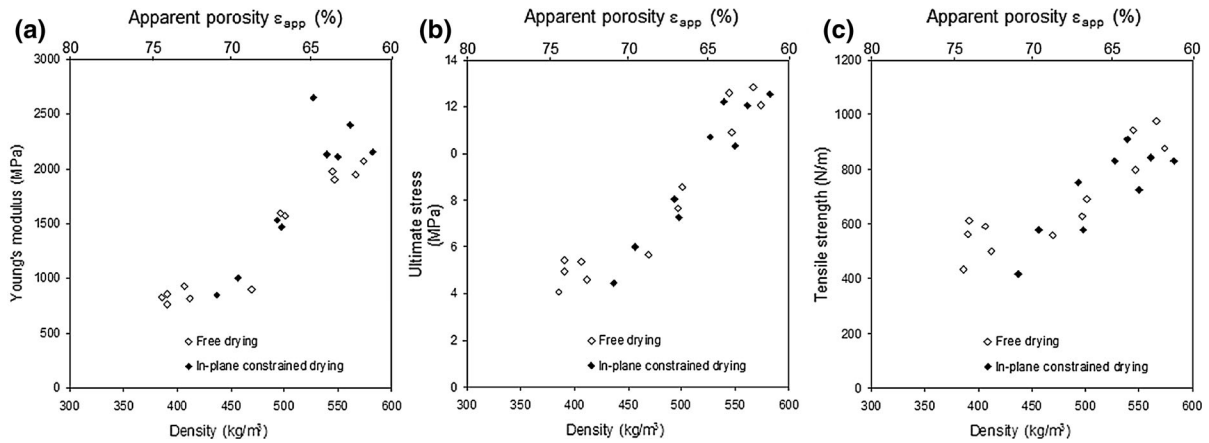

Fig. 5 Evolution of **a** the Young's modulus, **b** the ultimate stress σ_u and **c** the tensile strength T as a function of the apparent density ρ_{app} for the in-plane isotropic papers

whereas the porosity ϵ_X could capture local microstructural changes inside rather small gauge zones of approximately 2 mm in diameter. However, the general evolution of ϵ_X shows that the scanned specimens captured the consolidation effect that was induced on the fibrous microstructure and consequently on the fibres and the fibre-to-fibre bonds by the increase in the packing stress.

Mechanical behaviour

Figure 5 shows that an increase in the apparent density, i.e., a decrease in the porosity, had a predominant effect on the increase in the Young's modulus, the ultimate stress or the tensile strength of in-plane isotropic papers, which is commonly observed for papers. For instance, an increase in the apparent density from approximately 400 to 550 kg m^{-3} led to an increase in the Young's modulus that ranged between approximately 700 and 2500 MPa, whereas the increase in the ultimate stress ranged between approximately 4 and 12 MPa. Besides the drying operation did not have an obvious effect on the mechanical properties of model papers. In contrast, wet pressing was the operation that predominantly affected the paper mechanical properties because of its

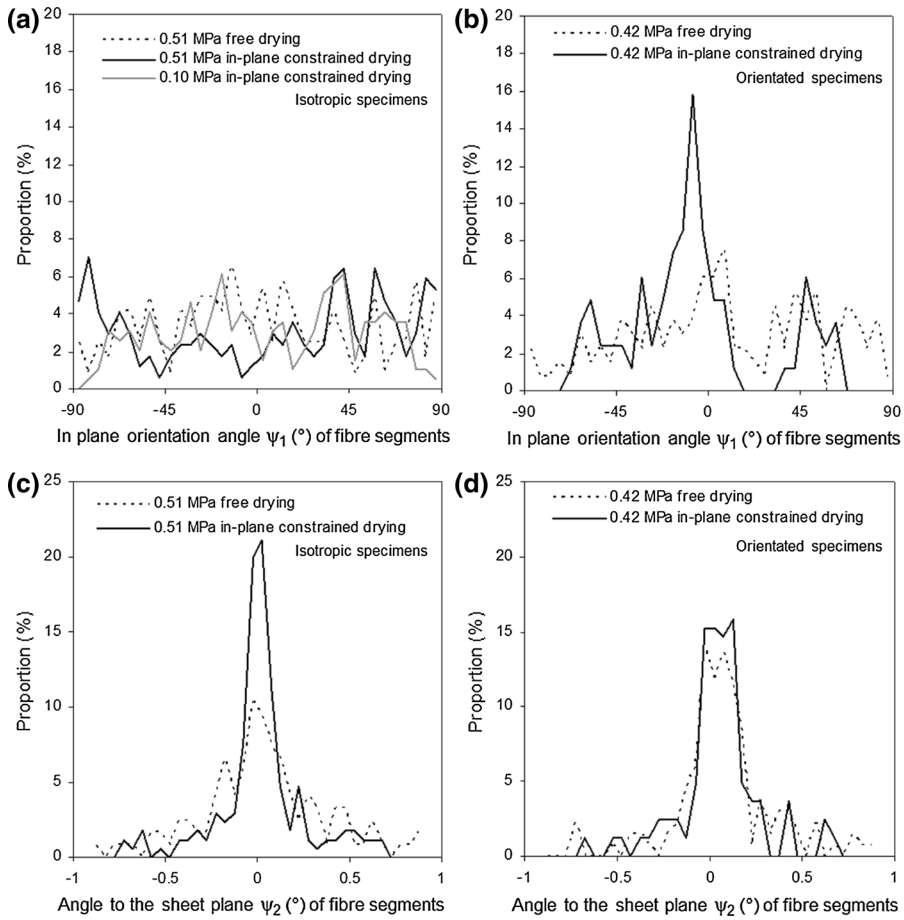

Fig. 6 Distributions of the angles ψ_1 and ψ_2 for **a** the in-plane isotropic specimens and **b** the in-plane orientated specimens. The interval size used to plot these distributions was set to 5° and 0.05° for ψ_1 and ψ_2, respectively

Table 1 Mean out-of-plane angle $\langle \Psi_2 \rangle$ and related standard deviation of σ_{Ψ_2} obtained for various forming, pressing and drying conditions

Forming	Isotropic				Orientated			
Packing stress (MPa)	0.10		0.51		0.11		0.42	
Drying conditions	F	P	F	P	F	P	F	P
Standard deviation σ_{Ψ_2} (°)	–	0.5	2.4	0.6	1.7	0.4	1.8	0.6

The letters F and P stand for free and in-plane drying conditions, respectively

indirect effects on the consolidation of the paper fibrous network and on the apparent density ρ_{app} (Niskanen and Krenlampi 1998). However, the ultimate stress and tensile strength of the studied model papers were low, which was certainly related to low mechanical properties of fibre-to-fibre bonds because of the use of unbeaten fibres.

Fibrous structure at the fibre scale

Fibre centrelines

The distributions of the in-plane orientation angle ψ_1 are shown in Fig. 6a, b for the isotropic and orientated specimens of model papers, respectively. For the

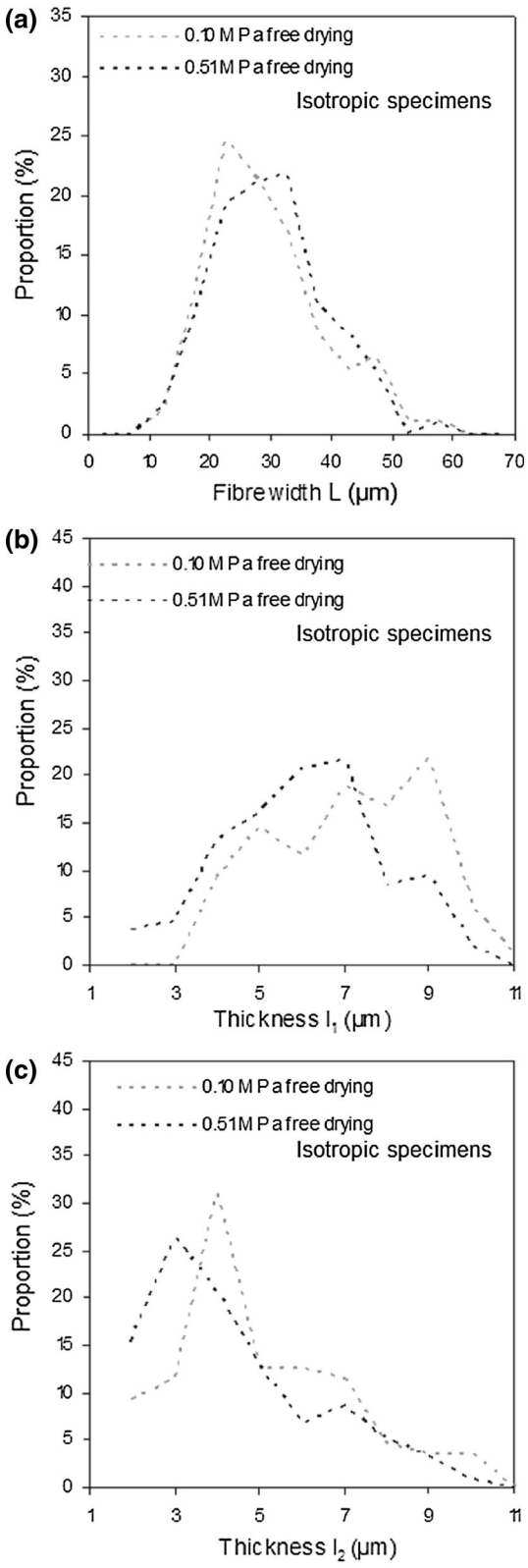

◀**Fig. 7** Distributions of **a** the fibre width L, **b** the thickness l_1 and **c** the thickness l_2 of the fibre cross sections for in-plane isotropic specimens. The interval sizes used to plot these distributions were set to 5 µm for L and 1 µm for l_1 and l_2, respectively

isotropic specimens, the distributions were flat. Consequently, the fibre segments did not have any preferential orientation for all pressing or drying conditions. On the contrary, the fibre segments of the orientated specimens (Fig. 6b) exhibited a preferential orientation that was clearly marked around the 0°-direction for the specimens that were dried under constraint. These distributions roughly exhibited the same shape and the same orientation intensity per orientation class as the typical fibre orientation distributions, shown in Fig. 1e. This result is astonishing as the distributions shown in Fig. 6a, b were built using a low number of segments compared to that of the distributions that were determined using a macroscopic method in Fig. 1e, f.

Figure 6c, d shows the distributions for the out-of-plane orientation angle ψ_2 that were determined for the isotropic specimens and for low and high wet pressing conditions, respectively. Figure 6e, f shows the same distributions for the orientated specimens. These symmetric distributions exhibited a pronounced peak that was centered around the 0°-direction, showing that the fibre segments predominantly lay in the $(\boldsymbol{e}_1, \boldsymbol{e}_2)$-plane of the handsheets, i.e., the main plane of the images, or close to that plane. Note also the decrease in the standard deviation of the angle Ψ_2 for constrained drying compared to that measured for free drying regardless of the orientation of the specimens (see Table 1), showing that the in-plane orientation of the fibre segments was more pronounced for constrained drying than free drying.

Fibre cross sections

Width

Figure 7a shows a typical example of fibre width distributions that were determined for the isotropic and orientated specimens. An increase in the wet pressing conditions shifted the fibre width distributions towards higher values for all drying conditions.

Data given in Table 2 for the mean width $\langle L \rangle$ and the ratio of the standard deviation to the mean fibre width $\sigma_L / \langle L \rangle$ also illustrate the effects of wet pressing

Table 2 Mean width $\langle L \rangle$, thickness $\langle l_1 \rangle$, thickness $\langle l_2 \rangle$ and inclination angle $\langle \theta \rangle$ of the fibre cross sections obtained for various forming, pressing and drying conditions, and related standard deviations or normalised standard deviation of these parameters

Forming	Isotropic				Orientated			
Packing stress (MPa)	0.10		0.51		0.11		0.42	
Drying conditions	F	P	F	P	F	P	F	P
Mean width $\langle L \rangle$ (μm)	29.8	30.6	30.6	36.1	29.1	30.0	31.2	29.3
Standard deviation σ_L (μm)	9.3	8.6	8.7	9.8	12.7	15.9	10.4	10.0
$\sigma_L/\langle L \rangle$	31 %	28 %	28 %	27 %	44 %	53 %	33 %	34 %
Mean thickness $\langle l_1 \rangle$ (μm)	7.7	6.8	6.5	6.3	5.8	5.1	4.8	4.9
Standard deviation σ_{l_1} (μm)	1.8	2.0	1.9	1.8	2.7	2.6	2.1	1.7
$\sigma_{l_1}/\langle l_1 \rangle$	23 %	29 %	29 %	29 %	47 %	51 %	44 %	35 %
Mean thickness $\langle l_2 \rangle$ (μm)	5.6	5.8	5.0	4.5	5.2	4.8	4.4	4.4
Standard deviation σ_{l_2} (μm)	2.2	1.8	2.1	1.3	3.3	2.8	2.3	1.4
$\sigma_{l_2}/\langle l_2 \rangle$	39 %	31 %	42 %	29 %	63 %	58 %	52 %	32 %
Mean inclination angle $\langle \theta \rangle$ (°)	1.81	−1.76	0.77	0.03	4.2	0.9	0.3	−1.6
Standard deviation σ_θ (°)	18.0	20.4	11.4	14.1	25.6	29.4	16.1	16.3

The letters F and P stand for free and in-plane drying conditions, respectively

and drying conditions as well as of fibre orientation on the variations in the fibre width.

For the isotropic and freely dried specimens, an increase in wet pressing resulted in a weak increase in the mean fibre width $\langle L \rangle$. A maximum 18 %-increase in the mean fibre width was measured for the isotropic specimens that were dried under constraint between the lowest and highest packing stresses. An increase in wet pressing had a similar effect on the mean fibre width of the orientated and freely dried specimens. However, similar phenomena were not observed for the orientated specimens that were dried under constraint.

The ratio $\sigma_L/\langle L \rangle$, which represents the scattering of the fibre width, gives a better understanding of the effects of wet pressing. For both the isotropic and orientated specimens and for all drying conditions, the higher the packing stress during wet pressing, the lower was this ratio, which shows that the fibre width was homogenised in the fibrous networks.

The mean fibre width of isotropic and orientated specimens was similar. However, the ratio $\sigma_L/\langle L \rangle$ was larger for the orientated specimens compared to the isotropic specimens, regardless of the pressing and drying conditions. This behaviour could be easily observed for equivalent low pressing conditions for both isotropic specimens (0.10 MPa) and orientated specimens (0.11 MPa). The effect of drying on the ratio $\sigma_L/\langle L \rangle$ was not obvious. For the isotropic specimens, a slight decrease in this ratio was measured. But this trend was not observed for the orientated specimens, especially for the lowest pressing condition.

Thickness l_1

Figure 7b shows a typical distribution for the thickness l_1. An increase in wet pressing induced a decrease in the thickness l_1. The evolution of the mean values $\langle l_1 \rangle$ given in Table 2 confirmed this result. Drying conditions had an effect on the mean value of the thickness $\langle l_1 \rangle$, which was lower for constrained drying than free drying. This effect was less pronounced for the highest wet pressing conditions and nearly disappeared for orientated specimens. The mean thickness $\langle l_1 \rangle$ was lower for orientated specimens than isotropic specimens. The ratio $\sigma_{l_1}/\langle l_1 \rangle$ was also higher for orientated specimens than isotropic specimens, showing that the heterogeneity of this fibre property was related to the fibre orientation in the studied fibrous networks. Note also that wet pressing and drying conditions did not have any clear effect on the evolution of the ratio $\sigma_{l_1}//\langle l_1 \rangle$.

Thickness l_2

The thickness l_2, the mean values of $\langle l_2 \rangle$ and the ratios $\sigma_{l_2}/\langle l_2 \rangle$ decreased as the packing stress increased

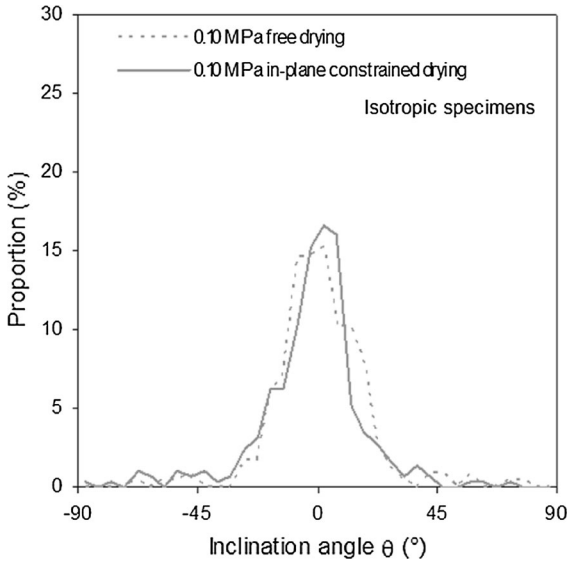

Fig. 8 Distribution of the inclination angle θ of the fibre cross sections for in-plane isotropic specimens. The interval size used to plot these distributions was set to 5°

during wet pressing for all the investigated drying conditions (see Fig. 7c and data given in Table 2). The effect of drying conditions on l_2 was not obvious for the isotropic specimens. In contrast, the decrease in $\sigma_{l_2}/\langle l_2 \rangle$ for constrained drying compared to free drying showed that constrained drying homogenised this property for the orientated specimens. Note also that this ratio was larger for the orientated specimens than the isotropic specimens, suggesting an increase in the heterogeneity of this property for the orientated specimens.

Inclination angle θ

The distributions of the inclination angle θ of the major axis of the fibre cross section (see a typical example in Fig. 8) showed that the major axes were mostly parallel to the plane of the handsheets. Note also that the mean values $\langle \theta \rangle$ were not exactly zero (see Table 2). This effect could be attributed to the slight inclination of the main plane of the paper specimens compared to the $(\boldsymbol{e}_1, \boldsymbol{e}_2)$-plane of the X-ray microtomography frame. This inclination was very limited.

Interestingly, note that the peaks of the distributions were higher for high wet pressing conditions compared to low wet pressing conditions (see also the decrease in the standard deviation of θ in Table 2). Thus, the increase in the packing stress σ_0 had the effect of decreasing the inclination angle of the fibre cross sections, suggesting that their main axes was more parallel to the midplane of the specimens and showing that this property was more homogeneous.

In addition, data in Table 2 shows that constrained drying induced a slight increase in the heterogeneity of this property compared to free drying. Note also the high standard deviation σ_S for the orientated specimens, which shows a more heterogeneous inclination angle distribution than the isotropic specimens.

Fibre-to-fibre contacts/bonds

Distance between contacts

Figure 9a shows the evolution of the number of picked contacts on the shape of the distributions of the inter-bond distance Δs. For a relatively low number of picked contacts, the distributions astonishingly appeared to be rather stable. This stabilisation is better illustrated in Fig. 9b: approximately 60 contacts were sufficient to obtain the stabilisation of the mean and the standard deviation of Δs, i.e., to obtain a representative information for this parameter.

The general aspect of these distributions was the same for all investigated forming, pressing, and drying conditions. In addition, data in Table 3 shows that the orientated specimens exhibited a larger mean inter-bond distance $\langle \Delta s \rangle$ than the isotropic specimens for comparable pressing and drying conditions. For both the isotropic and orientated specimens, the increase in the packing stress during wet pressing was also accompanied by a decrease in the mean inter-bond distance $\langle \Delta s \rangle$ regardless of the drying conditions. For the isotropic specimens, the medians of the distributions of the inter-bond distance Δs were not affected by the wet pressing conditions. On the contrary, an increase in the wet pressing conditions resulted in a decrease in the medians of the inter-bond distance for the orientated specimens. Thus, the shape of the distributions was not largely affected by wet pressing for the isotropic specimens, whereas the contrary effect appeared to have been introduced for the orientated specimens. For the isotropic specimens, an increase in the wet pressing conditions was also accompanied by an increase in $\sigma_{\Delta s}/\langle \Delta s \rangle$, corresponding to a more heterogeneous inter-bond distance Δs, whereas the contrary effect was observable for the orientated specimens. The micromechanisms that were at the

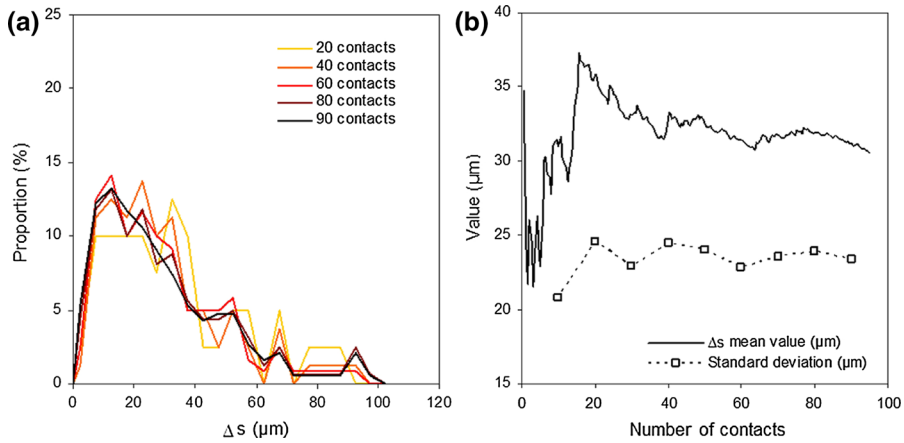

Fig. 9 **a** Distributions of the inter-bond distances Δs as a function of the number of randomly picked contacts. **b** Mean values and standard deviations of these distributions as a function the number of randomly picked contacts. These measurements were made within a scanned volume of 140 μm × 140 μm × t for an in-plane isotropic paper subjected to a packing stress of 0.51 MPa and to constrained drying

Table 3 Mean distance between the centres of two consecutive bonds $\langle \Delta s \rangle$, ratio between bonded width and fibre width $\langle l_i/L \rangle$ and surface of bonds $\langle S \rangle$ obtained for various forming, pressing and drying conditions, and related standard deviations, normalised standard deviation and median of these parameters

Forming	Isotropic				Orientated			
Packing stress (MPa)	0.10		0.51		0.11		0.42	
Drying conditions	F	P	F	P	F	P	F	P
Mean inter bond distance $\langle \Delta s \rangle$ (μm)	–	35.8	20.7	30.6	42.8	49.7	30.3	34.0
Standard deviation $\sigma_{\Delta s}$ (μm)	–	21.8	15.9	23.1	42.1	28.2	19.9	19.6
$\sigma_{\Delta s}/\langle \Delta s \rangle$	–	61 %	77 %	75 %	98 %	57 %	66 %	58 %
Median (μm)	–	42.0	27.3	43.4	60.1	54.2	37.0	41.6
Mean bonding degree ratio $\langle l_i/L \rangle$ (%)	–	31	42	41	29	29	34	38
Standard deviation $\sigma_{l_i/L}$ (%)	–	26	25	32	23	23	26	32
$\sigma_{l_i/L}/\langle l_i/L \rangle$	–	84 %	60 %	78 %	79 %	79 %	76 %	84 %
Median (%)	–	52.2	56.2	59.1	42.6	39.4	47.2	55.2
Mean bond surface area $\langle S \rangle$ (μm^2)	–	375	385	483	260	426	419	590
Standard deviation σ_S (μm^2)	–	466	596	1111	378	591	604	960
$\sigma_S/\langle S \rangle$	–	124 %	155 %	230 %	145 %	139 %	144 %	163 %
Median (μm^2)	–	593	519	611	599	775	605	718

The letters F and P stand resp. for free and in-plane drying conditions

origin of these differences should be further investigated.

In addition, the drying conditions affected the inter-bond distance Δs for the highest pressing: constrained drying induced larger inter-bond distances Δs compared to free drying. This difference could be attributed to a stretching effect of the inter-bond segments, which may occur during constrained drying, whereas free drying would enable a pronounced shrinkage of the inter-bond segments. Note that the inter-bond distance did not have the same evolution for the orientated specimens that were fabricated using the lowest wet pressing conditions.

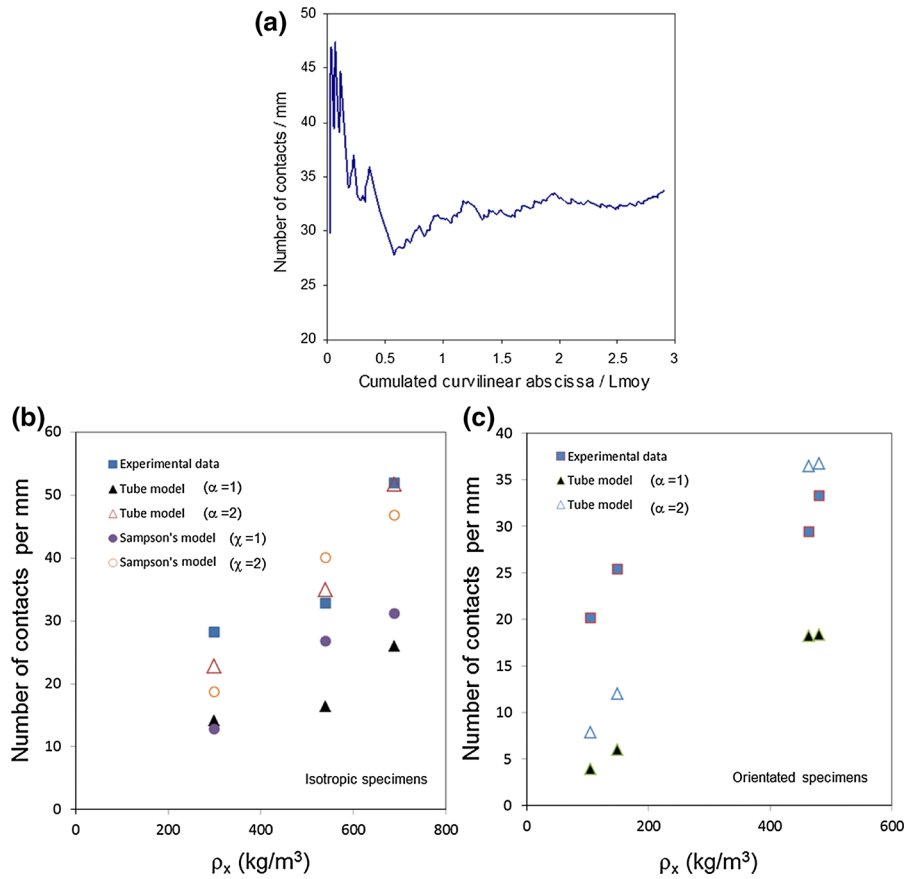

Fig. 10 **a** Experimental number of contacts per unit of fibre length as a function of the cumulated curvilinear abscissa normalised by the mean length of the fibres. Comparison between the number of contacts per unit of fibre length experimentally measured and estimated using the tube model and Sampson's model for the in-plane isotropic specimens (**b**) and the orientated specimens (**c**)

Interestingly, note that the mean inter-bond distance $\langle \Delta s \rangle$ was of the same order as the mean fibre width $\langle L \rangle$ for all specimens (see Table 2), which shows that the investigated fibrous networks were highly connected despite their rather low grammage and density.

Mean number of contacts per fibre

The mean number of contacts per unit of fibre length was estimated using the data for the mean inter-bond distance. Figure 10a shows the number of contacts per unit of length as a function of the normalised cumulated curvilinear abscissa calculated by randomly summing all the inter-bond distances that were measured along all examined fibre segments inside a volume. A stabilised number of contacts per unit of length (of approximately 30 for this example) was reached for a normalised cumulated curvilinear abscissa of approximately one, i.e., corresponding to a mean fibre length L_{moy}. The same observation was made for all the investigated microstructures. This important result shows that a representative number of contacts can be determined using volumes of fibrous networks having a limited size.

Figure 10b, c shows the evolution of the experimental mean number of contacts per unit of fibre length as a function of the density ρ_X or the porosity ϵ_X for all investigated specimens. The increase in the number of contacts per unit length was 85, 60 %, over the range of ϵ_X for the isotropic and orientated specimens, respectively.

Bonding degree ratio

A typical example of a distribution of the bonding degree ratio l_i/L is shown in Fig. 11a. The shape of the distributions was similar for all drying and pressing conditions. These distributions showed that the major part of the bonds between fibres were partial ($l_i/L < 100$ %). Note also that few values of l_i/L could be >100 % because the fibre width was measured in one position along the fibre centreline.

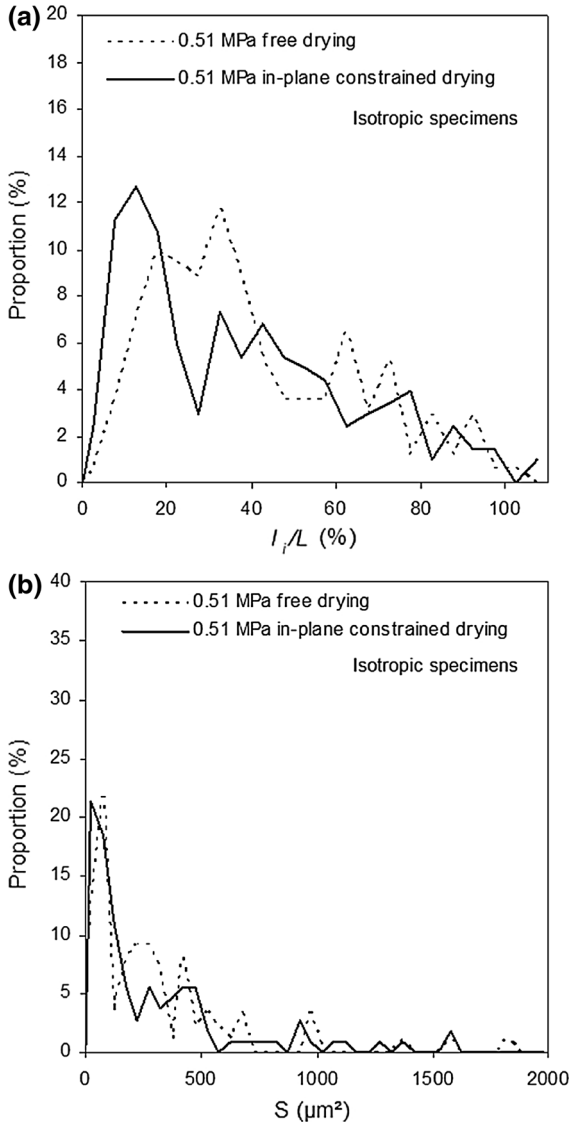

Fig. 11 **a** Distributions of the bonding degree ratio l_i/L and **b** the bond surface area S for the in-plane isotropic specimens. The interval size used to plot these distributions was set to 5 % for l_i/L and 50 µm^2 for S

The most important and original result is given in Table 3: the mean bonding degree ratio $\langle l_i/L \rangle$ was low and ranged only between approximately 30 and 40 % for all the investigated specimens. However, wet pressing had a clear effect on the bonding degree ratio l_i/L, regardless of drying conditions: an increase in the packing stress σ_0 resulted in an increase in $\langle l_i/L \rangle$. Drying also affected the bonding degree ratio as, for the highest pressing conditions, the scattering coefficient $\sigma_{l_i/L}/\langle l_i/L \rangle$ was lower for free drying ($\sigma_{l_i/L}/\langle l_i/L \rangle = 60$ % for $\sigma_0 = 0.51$ MPa) than constrained drying ($\sigma_{l_i/L}/\langle l_i/L \rangle = 78$ % for $\sigma_0 = 0.51$ MPa), showing that free drying resulted in an increased homogeneity of the geometry of bonds. The effect of wet pressing on the heterogeneity of the bonding degree ratio was unclear as the evolution of the scattering coefficient $\sigma_{l_i/L}/\langle l_i/L \rangle$ did not exhibit any clear tendency for both the isotropic and orientated specimens.

Bond surface area

Figure 11b shows a typical example of a distribution of the bond surface area S for the isotropic and orientated specimens. Note that the calculations of this parameter was enhanced compared to a previous study (Marulier et al. 2012) because the number of scrutinised bonds was increased. However, the evolution of S as a function of σ_0 was similar in both studies, i.e., an increase in σ_0 resulted in an increase in S. In addition, the bond surface area S remained below approximately 2000 µm^2. Note also the pronounced scattering $\sigma_S/\langle S \rangle$ of the bond surface area S for all specimens.

The mean bond surface areas were close for all the specimens that were fabricated using similar pressing and drying conditions (see Table 3). However, the median values of the bond surface area were greater for the orientated specimens compared to the isotropic specimens (see Table 3). This result demonstrated that the number of bonds having a large surface was larger in the orientated specimens compared to the isotropic specimens. An increase in wet pressing resulted in an obvious increase in the bond surface area S (see the mean values for S in Table 3). Constrained drying also resulted in larger bond surface areas compared to free drying (see Table 3). The origin of this phenomenon is not obvious considering the aforementioned low variations in the bonding degree ratio between drying conditions. However, constrained drying also induced larger fibre widths compared to free drying for all the investigated forming and wet pressing conditions.

Discussion

Paper microstructures

To the knowledge of the authors, few studies provided so many parameters for the morphology of fibres and

fibre-to-fibre contacts/bonds inside the microstructure of papers using a direct observation method. Page et al. (1962) studied the bond surface and the inter-bond distance and He et al. (2003) investigated the fibre morphology in fibre networks. These studies relied on an extensive and fine microscopy work. Usually, individual fibres or individual fibre-to-fibre bonds (Schmied et al. 2012, 2013; Fischer et al. 2012), have been studied. The results of this study were obtained using X-ray microtomography 3D images, which demonstrates the outstanding relevance of these images for revealing the internal 3D geometry of fibres and bonds in fibrous networks. These experimental results also contribute to enrich these former studies as new parameters such as the in-plane fibre orientation were also assessed.

The present study provided a relevant insight on the influence of manufacturing operations on the forming mechanisms of paper microstructures and more particularly on (1) the collapse of fibre cross sections, (2) the shape of fibre centrelines and the fibre orientation as well as (3) the fibre-to-fibre bonds.

The development of a ribbon-like shape for the fibres was accompanied by the collapse of the fibre cross sections. The increase in wet pressing had a clear effect on these morphological parameters as it resulted in both an increase in the width of the fibre cross sections and in an alignment of the main axis of the fibre cross sections parallel to the plane of the handsheets. The effect of drying conditions was less consistent. However, the shrinkage of the lateral thickness of the fibre cross sections was more pronounced for constrained drying than free drying. Note also that the influence of the in-plane orientation of fibres was weak. However, the dimensions of the fibre cross sections exhibited a higher scattering for in-plane orientated fibrous networks than for in-plane isotropic networks. He et al. (2003) have already reported that the collapse of the fibre cross sections is not uniform for in-plane isotropic networks. These authors attributed this effect to an uneven stress transfer, induced by the non-uniform structure of fibre networks and by the scattering in the collapsibility of fibres. These results are now completed for in-plane orientated networks into which the stress transfer could be all the more uneven as fibres have an in-plane preferential orientation.

Fibres can undergo twist, bending, stretching or shearing during network papermaking operations. The inclination angle θ of the fibre cross sections can be related to the torsion of fibres that results from manufacturing operations. Results showed that an increase in wet pressing reduced both the fibre torsion and its heterogeneity. Likewise, the torsion of fibres was more heterogeneous for in-plane orientated networks than in-plane isotropic networks. Fibre bending (see the angle Ψ_2) was also lower for constrained drying than free drying. These two examples show how fibres are constrained during wet pressing or drying. But note that the reported effects were not pronounced.

Knowing the geometry of fibre-to-fibre bonds within fibrous networks is crucial for the prediction the physical and mechanical properties of fibrous networks. The observations that fibre-to-fibre bonds were partial were in accordance with the observations of the impressive study by Page et al. (1962) on fibre-to-fibre bonding. The estimated bond areas were also in accordance with those of this former study. The most important parameters to induce variations in the degree of bonding were wet pressing and in-plane fibre orientation. Likely constrained drying had also a slight beneficial effect as this drying could induce an increase in the degree of bonding.

The physical and mechanical properties of fibre networks also greatly depend on the number of fibre-to-fibre contacts/bonds. In this study, we obtained two original and important results for this property. The first important result was that a representative number of fibre-to-fibre contacts/bonds can be determined using volumes that must contain enough fibres or fibre segments the cumulated length of which is equal to the mean fibre length. This result is important as it shows that a representative elementary volume (REV) for the number of fibre-to-fibre contacts/bonds has rather small dimensions. The second important result was obtained for the evolution of the evolution of the mean number of contacts per unit of fibre length as a function of the density (or porosity). Few similar results were found in the literature for the variations in the number of contacts per fibre (or per unit of fibre length) as a function of the paper density. Batchelor et al. (2006) reported similar results for in-plane isotropic laboratory papers using a cross-sectional grinding technique. However, for the in-plane orientated papers, the results that were obtained using X-ray microtomography images are original to the knowledge of the authors.

Statistical distributions

The experimental distributions for the morphology of the fibres and bonds, i.e., L, l_1, l_2, Δs, l_i/L and S, were fitted by Weibull distributions. For the width distribution, the relevancy of the use of Weibull distributions was already demonstrated by Seth et al. (2003). For the parameters l_1, l_2, and l_i/L and S, the Weibull distribution enables a correct description of these morphological parameters. For the bond inter-bond distance Δs, this distribution gives a good description of the experimental results. As theoretically proposed by Sampson (2009b), gamma distributions could also be used to describe the inter-bond distance. The probability density function and the cumulative distribution function of this distribution write, respectively, as follows:

$$\forall x \geq 0, \quad f(x) = \frac{c}{b}\left(\frac{x}{b}\right)^{c-1} \exp\left(-\left(\frac{x}{b}\right)^{c}\right) \quad \text{for } x \geq 0, \tag{7}$$

and

$$F(x) = 1 - \exp\left(-\left(\frac{x}{b}\right)^{c}\right), \tag{8}$$

where $b > 0$ and $c > 0$.

Two methods were used to determine the scale parameter b and the shape parameter c. The first method consisted of a least-squares regression technique to identify both the parameters b and c, whereas the second method consisted of taking the parameter b to be the experimental mean value of the distributions and determining c by a least-squares method. The as-determined morphological parameters are given in Table 4, where b_1 and c_1 are the parameters corresponding to the first method and b_2 and c_2 are the parameters corresponding the second method. Examples of fitted distributions are shown in Fig. 12a–d. Both fitting methods well approximated the experimental distributions for all parameters, except for the fibre width L. In this case, the least-squares method induced a shift of the mean fibre width that was quite important ($\approx$5 μm).

The data given in Table 4 could be used to assess the effectiveness of the numerical generator of fibrous networks that are currently in development to mimic paper-like microstructures.

Relative bonded area (RBA)

The RBA_X was estimated using the experimental results of this study for each investigated volume. The major axis of the fibre cross sections was considered to be parallel to the midplane of the handsheets (see for example Fig. 8), which suggests that the available surfaces for bonding were the upper and lower sides of the fibres. Noting s_{max} the maximum curvilinear abscissa and $\langle L_i \rangle$ the mean width of fibre i, the total bonding surface area of fibre i was approximated as

$$A_{T_i} = 2 s_{max_i} \langle L_i \rangle. \tag{9}$$

In addition the bonding area $S_j^{(i)}$ of each bond j of fibre i was estimated for all the fibre-to-fibre bonds. Consequently, RBA_X was estimated for each volume as follows:

$$RBA_X \approx \frac{\sum_{i=1}^{i=N} \sum_{j=1}^{j=n_i} S_j^{(i)}}{\sum_{i=1}^{i=N} A_{T_i}}, \tag{10}$$

where N is the number of fibres and n_i the number of contacts of fibre i.

Figure 13a shows the evolution of RBA_X as a function ρ_X. RBA_X ranged between approximately 0.1 to 0.3 between $\approx$100 and $\approx$700 kg m^{-3}. Note also that RBA_X for the orientated specimens was of the same order as for the isotropic specimens. This result shows that in-plane fibre orientation has a minor influence of the RBA, which is in accordance with theoretical predictions of Sampson's model (Sampson 2009b).

These local estimates are in accordance with values of RBA that have already been reported by several authors. Page et al. (1962) found a RBA of approximately 0.16 for handsheets made up of unbeaten sulphite pulp (the paper density was not reported). Niskanen and Rajatora found RBAs of 0.13 and 0.17 (Niskanen and Rajatora 2002) for unbeaten or slightly beaten softwood kraft fibres. However, these values were considered to be low for the paper effective densities that ranged between 662 and 860 kg m^{-3} (Niskanen and Rajatora 2002; Sampson 2004). The RBAs of this study were of the same order as those measured for handsheets made up of kraft pulp by Yang et al. (1978). These authors found RBAs that ranged between 0.3 and 0.5 between 500 and 700 kg m^{-3}. The RBAs of this study were also in

Table 4 Parameters b_1, c_1 and b_2, c_2 of the Weibull distributions for L, l_1, l_2, Δs, l_i/L and S obtained for various forming, pressing and drying conditions

Forming	Isotropic				Orientated			
Packing stress (MPa)	0.10		0.51		0.11		0.42	
Drying conditions	F	P	F	P	F	P	F	P
L								
b_1 (μm)	34.0	35.0	35.0	41.0	34.5	34.5	36.5	34.0
c_1	3.8	3.9	4.1	4.0	2.6	2.5	3.6	3.4
$b_2 = \langle L \rangle$ (μm)	29.8	30.6	30.6	36.1	29.1	30.0	31.2	29.3
c_2	4.4	4.0	4.4	4.2	2.6	2.5	3.7	3.8
l_1								
b_1 (μm)	7.4	6.2	6.2	5.8	5.6	5.0	4.8	4.8
c_1	3.9	3.1	3.3	3.2	2.4	5.1	2.2	3.0
$b_2 = \langle l_1 \rangle$ (μm)	7.7	6.8	6.5	6.3	5.8	5.2	4.8	4.9
c_2	3.8	2.8	3.2	2.9	2.4	1.9	2.2	2.9
l_2								
b_1 (μm)	5.0	5.1	4.3	3.9	4.3	4.3	4.2	4.1
c_1 (μm)	2.3	2.7	1.9	2.8	2.6	2.1	2.5	2.4
$b_2 = \langle l_2 \rangle$ (μm)	5.6	5.8	5.0	4.5	5.2	4.8	4.4	4.4
c_1 (μm)	2.2	2.4	1.8	2.5	2.1	1.9	2.4	2.3
Δs								
b_1 (μm)	–	34.0	18.5	28.5	32.0	47.5	30.0	34.0
c_2	–	1.6	1.3	1.2	1.2	1.8	1.5	1.8
$b_2 = \langle \Delta s \rangle$ (μm)	–	35.8	20.7	30.6	42.8	49.7	30.3	34.0
c_2	–	1.7	1.4	1.4	1.4	2.0	1.5	1.8
l_i/L								
b_1 (%)	–	30	43	38	27	27	33	33
c_1	–	1.0	1.6	1.2	1.1	1.1	1.2	1
$b_2 = \langle l_i/L \rangle$ (%)	–	31	42	41	29	29	34	38
c_2	–	1.1	1.5	1.3	1.0	1.0	1.3	1.3
S								
b_1 (μm^2)	–	238	264	227	155	271	248	294
c_1	–	0.7	0.9	0.7	0.5	0.7	0.7	1.0
$b_2 = \langle S \rangle$ (μm^2)	–	375	385	483	260	426	419	590
c_2	–	0.9	1.0	0.9	0.8	0.8	0.9	1.1

The letters F and P stand for free and in-plane drying conditions, respectively

accordance with the results of Paavilainen (1994). Thus the present experimental results are reliable even if several rough assumptions were used to model the fibre surface and estimate the bond surface area.

Note also that Fig. 13a shows the evolution of the RBAs that were estimated using the method of Ingmanson and Thode (1959) as a function of the apparent density ρ_{app}. In this approach, the scattering coefficient ϑ_c is considered to be correlated to the tensile strength T (see Fig. 13b). The extrapolation of ϑ_c at $T = 0$ provides ϑ_{c0}, i.e., the scattering coefficient for a completely unbonded sheet, and consequently the total surface of fibres. Batchelor and He (2005) and Batchelor et al. (2008) have underlined that it is difficult to obtain a good extrapolation for the scattering coefficient using this method. Therefore, the results of this method are often questionable. In this study, the extrapolation function was assumed to

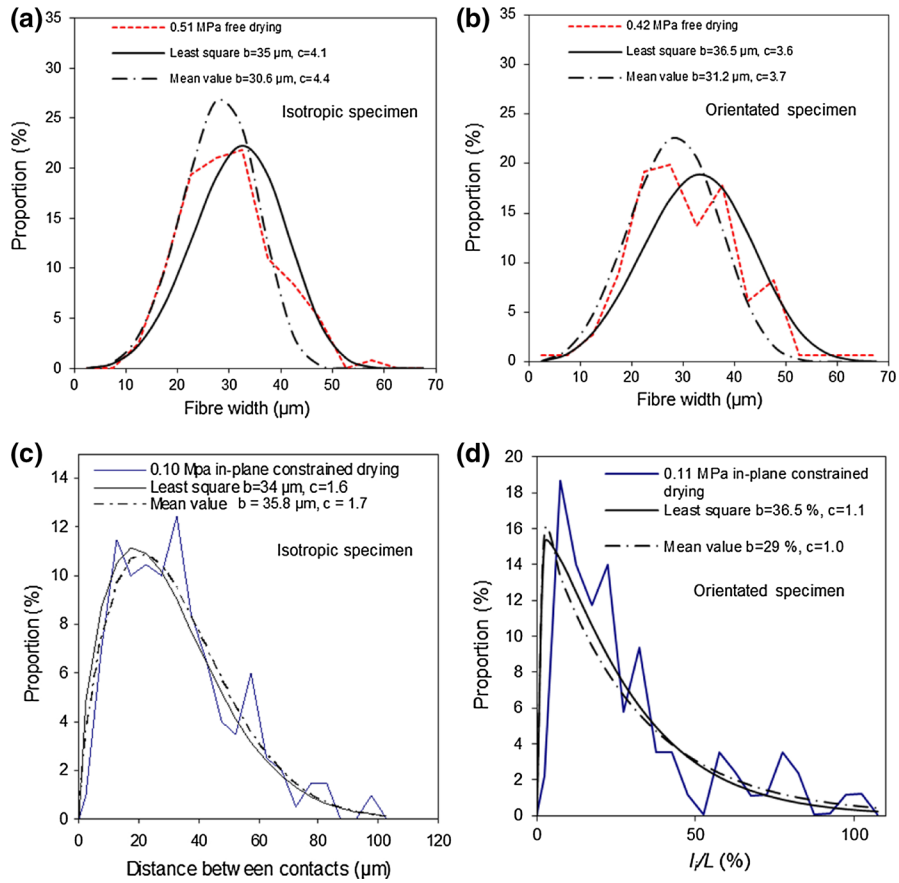

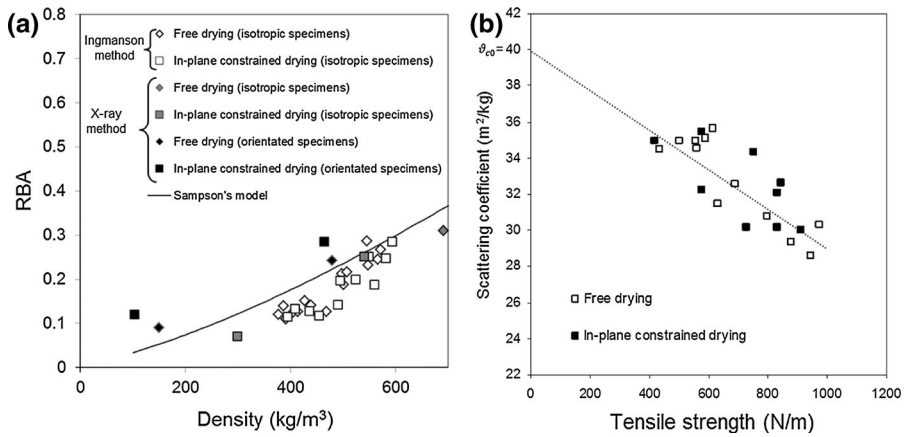

Fig. 12 Weibull distributions for **a**, **b** the fibre width, **c** the distance between contacts and **d** the bonding degree ratio. In these figures, note that the Weibull probability density functions were discretised into bins of the same size as those representing the experimental data

Fig. 13 RBA as a function of the paper density. **a** RBA estimated using X-ray microtomography data (in this case, the density was the effective density ρ_X) and **b** the method of Ingmanson and Thode (density ρ_{app}). **b** Light scattering coefficient ϑ_c as a function of the tensile strength T: experimental values and linear fit. Note that Sampson's model was here estimated using the following averaged parameters: fibre width $\omega = 30$ µm, fibre length $\lambda = 2$ mm

be linear, considering the data that have been reported by Ingmanson and Thode (1959) for classified and unbeaten pulps. The extrapolated scattering coefficient ϑ_{c0} was 40 m^2 kg^{-1}. The RBAs were obtained for the in-plane isotropic handsheets using the as-estimated parameter ϑ_{c0} and measured ϑ_c. No

distinction was made between the drying conditions for the RBAs that are shown in Fig. 13a. Globally, the RBA sharply increased for densities over 400 kg m^{-3}, whereas it did not exhibit any pronounced changes for lower densities. This result is in accordance with the observations of Ingmanson and Thode (1959). In addition the RBA ranged between ≈0.1 and ≈0.3 for apparent densities ρ_{app} between approximately 400 and approximately 600 kg m^{-3}. Hence, the values of RBA were of the same order using the local and global experimental methods.

Assessment of the number of fibre-to-fibre contacts/bonds

The predictions of two models for the number of fibre-to-fibre contacts/bonds per fibre within a fibrous network were compared to the experimental results. The simplest model was the tube model (Toll 1993), commonly used in the fields of fibre suspensions and composite materials (Toll 1998; Corre et al. 2005; Vassal et al. 2008; Latil et al. 2011; Guiraud et al. 2012; Orgéas et al. 2012). In this model, fibres are considered to be straight and homogeneously distributed in space. Fibres can also overlap (soft core assumption). Guiraud et al. (2012) have shown that for fibres with planar fibre orientation ($\theta = 0$), identical elliptical cross sections of major axis d_{max} and minor axis d_{min} and identical length λ, the tube model describes the average number of fibre-to-fibre contacts $\bar{n}$ as a function of the porosity ϵ and the in-plane orientation of fibres as follows:

$$\bar{n} = \tilde{n}\pi\alpha d_{min} d_{max} \lambda \left(\frac{2}{\pi} \frac{\lambda}{d_{max}} \varphi_1 + \varphi_2 + 1 \right), \tag{11}$$

where $\tilde{n}$ is the number of fibre centre points per unit of volume and α a parameter used to define the size of the cross section of the tube with respect to the size of the cross section fibre ($\alpha = 1$ when both cross sections are equal). This equation can also be written as follows:

$$\bar{n} = 4\alpha(1-\epsilon) \left(\frac{2}{\pi} \frac{\lambda}{d_{max}} \varphi_1 + \varphi_2 + 1 \right). \tag{12}$$

The parameters ϵ, λ and d_{max} were taken as follows: $\epsilon = \epsilon_X$, $\lambda = L_{moy}$ and $d_{max} = \langle L \rangle$. The functions φ_1 and φ_2 given in Eq. 12 only depend on the fibre orientation. These parameters were estimated using the following discrete expressions:

$$\varphi_1 = \frac{1}{N^2} \sum_{i=1}^{N} \sum_{k=1}^{N} \| \boldsymbol{p}_i \times \boldsymbol{p}_k \|, \tag{13}$$

and

$$\varphi_2 = \frac{1}{N^2} \sum_{i=1}^{N} \sum_{k=1}^{N} | \boldsymbol{p}_i \cdot \boldsymbol{p}_k |, \tag{14}$$

where N is the number of picked fibres within the studied volumes. Note that for in-plane isotropic networks $\varphi_1 = \varphi_2 = 2/\pi$.

The microstructure model developed by Sampson (2004, 2009b) Batchelor et al. (2006), was also used. This model is based on a statistical description of the geometry of random fibre networks where the fibre centres are distributed according to a Poisson process and fibre axes are uniformly distributed. In this model the fibres are seen as rectangles of length λ and width ω and the number of contacts between fibres is computed by considering full crossing area. Note that in the studied model papers, full crossing areas are scarce (see for example the bonding degree ratio l_i/L). Sampson's model (Sampson 2009b) describes the number of contacts per fibre (considered to be rectangles of length λ and width ω) as follows:

$$\bar{n} = \chi \frac{\pi}{2} \frac{\lambda}{\omega} \phi_c, \tag{15}$$

where χ has been introduced to better fit the experimental results ($\chi = 1$ in the original Sampson's model) and ϕ_c is the fractional contact area of a network with mean coverage $\bar{c}$:

$$\phi_c \approx \left(1 - \frac{1}{\bar{c}} \right) \left(1 + \frac{\epsilon(2-(3-\epsilon)\epsilon)}{\ln \epsilon} \right) \tag{16}$$

and

$$\bar{c} = \frac{\omega \bar{\beta}}{\delta}. \tag{17}$$

The parameters of this model were taken as follows: $\epsilon = \epsilon_X$, $\lambda = L_{moy}$, $\omega = \langle L \rangle$, $\delta = 1.5 \times 10^{-4}$ g m^{-1} and $\bar{\beta} = 40$ g m^{-2}. Note that the fractional contact area ϕ_c is an estimate of the RBA . As shown in Fig. 13, Eq. 16 agrees very well with the experimental data.

The predictions of both models for the number of contacts $\bar{n}$ were compared to the experimental results for the in-plane isotropic papers in Fig. 10b and for the

in-plane orientated papers in Fig. 10c where the number of contacts was normalised by the average fibre length ($L_{moy} = 2$ mm). Only the tube model was compared to the experimental results for the orientated specimens.

When using the original Sampson's model ($\chi = 1$) and $\alpha = 1$ in the tube model, both model predictions underestimate the experimental data (see Fig. 10b, c).

When using $\alpha = 2$, the tube model well describes the experimental evolution of the number of contacts for in-plane isotropic specimens (see Fig. 10b). The tube model correctly describes the number of fibre-to-fibre contacts for the in-plane anisotropic and dense specimens (see Fig. 10c). In contrast, this model underestimates the number of contacts for the low-density in-plane orientated papers. The need for an increase in α from 1 to 2 is potentially related to the the geometry of fibres, for instance to the torsion and the bending of fibres.

Similarly, Sampson's model predictions are much better for $\chi = 1.5$. Batchelor et al. (2006) have already reported a similar result. These authors explained this problem in terms of the nature of fibre-to-fibre contacts. In Sampson's model, only "full" contact areas are considered; however the geometry of fibre-to-fibre contact in fibrous networks is extremely complex. To get rid of this problem, Batchelor et al. (2006) classified contacts into two groups: "partial" and "full" contacts. In this study no distinction was made between "partial" or "full" contacts. This could explain the differences between the Sampson model and the experiments when $\chi = 1$, which are shown in Fig. 10b.

This attempt at testing the predictions of several microstructure models shows that a precise description of the "real" geometry of the fibre-to-fibre contacts is needed. This objective is not yet fulfilled. A systematic classification of the geometry of fibre-to-fibre contacts could come out from progress in the analysis of 3D X-ray images of bonding zones. Otherwise confronting model predictions and experimental results for the number of fibre-to-fibre contacts is difficult.

Conclusion

The measurement of microstructure parameters at the scale of fibres and fibre-to-fibre bonds is difficult for fibrous materials such as papers. In this study, we used 3D images of model papers to build a database of microstructure descriptors for the complex fibre networks of model papers. The originality of this approach is that several microstructure descriptors were determined for the same set of papers using a unique observation technique. The investigated images were acquired using X-ray microtomography. The model papers were made up of classified softwood pulp fibres and fabricated by varying forming, wet pressing, and drying conditions. Descriptors such as the fibre orientation, the geometry of the fibre cross sections as well as the inclination of the fibre cross sections were quantified. The inter-bond distance and the number of fibre-to-fibre contacts/bonds per unit of fibre length and the bond surface area were also quantified.

- The present experimental results enables a better understanding of the effect of papermaking operations on the microstructure of paper: i.e., a better understanding of the deformation micromechanisms of fibres and bonds that are induced by these operations. These results demonstrated that wet pressing was the most important operation for the morphology of the fibrous networks, fibres and bonds. The increase in the packing stress during wet pressing induced a drastic decrease in the porosity, or conversely a noticeable increase in the fibre content. The increase in the packing stress also led the major axis of the fibre cross sections to be parallel to the main plane of the paper handsheets. In addition this increase induced a noticeable increase in the number of fibre-to-fibre contacts/bonds as well as a decrease in the distance between contacts/bonds. The forming operation governed the in-plane orientation of fibres and also induced appreciable variations in the morphology of fibres and bonds. For instance, the dimensions or the inclination of fibre cross sections were more dispersed for the in-plane anisotropic fibre networks than the in-plane isotropic networks. The in-plane anisotropic fibrous networks also contained more bonds having large dimensions. The effect of drying conditions was less appreciable, which could result from the use of unrefined fibres to fabricate the model papers. It would be interesting to perform the same type of analysis using papers made up of refined fibres to show a potential effect of drying conditions.

- The statistical evolution of several geometric properties for the fibres and the bonds was correctly represented using for example Weibull-like distribution functions. This result is interesting to test whether stochastic network generators correctly represent the complexity of fibrous materials such as papers.
- Another important result was that a representative estimate for the number of contacts/bonds per unit of fibre length could be obtained using volumes that have a rather limited size: a REV for this property must contain fibres or segments of fibres the cumulated length of which is of the same order as the mean fibre length.

We have also shown that the bond surface areas that were estimated using the present microstructure results were in accordance with data that have been reported in the literature. The estimated RBAs were also in accordance with experimental results obtained using a classical determination method. The microstructure Sampson's model for RBA also give correct predictions.

These results were also used to test whether microstructure models enable a correct prediction for the number of fibre-to-fibre contacts/bonds. Sampson's model for the number of contacts and the tube model underestimated the experimental data. For the tube model, this discrepancy could be related to the curliness and the torsion of fibres. The prediction was enhanced by increasing the size of the test tube around the fibres. For the Sampson's model, a fitting parameter was introduced to better fit the experimental data. In this case, the discrepancy is potentially related to the geometry of the contact surface.

Finally, the difficulties that are inherent to this type of analysis should be emphasised. The quality of the 3D X-ray microtomography images is crucial: the easier the segmentation, the easier is the measurement of the microstructure parameters. Recent progress in x-ray image acquisition techniques enhanced the quality of images and reduced segmentation problems. In this study, a visual analysis of the 3D images was performed. This approach is efficient but cumbersome. No automatic image analysis procedures can be used to routinely perform this type analysis for complex fibrous microstructures such as the investigated papers. However, Viguié et al. (2013) made recent and encouraging progress in the development of image analysis algorithms that enable the automatic identification of several descriptors (number, position, morphology and geometry) for individual fibres and fibre-to-fibre bonds in low density papers (15 g m^{-2}). The effectiveness of these types of algorithms should be tested and enhanced for denser papers that are for instance made of beaten pulp fibres.

Acknowledgments C. Marulier gratefully acknowledges the cluster MACODEV funded by the Région Rhône-Alpes for his PhD research grant. The authors also gratefully acknowledge the ESRF (beamline ID19, E. Boller) where the microtomography experiments were performed in the framework of the Long Term Project MA127 "Heterogeneous Fibrous Materials". The authors also gratefully acknowledge O. Guiraud (Novitom) for fruitful technical discussion. This work was partially carried out within the ANR research program "3D discrete analysis of deformation micro-mechanisms in highly concentrated fibre suspensions" (ANAFIB, Grant Agreement No. ANR-09-JCJC-0030-01). This work was also partially carried out within PowerBonds, a project funded by WoodWisdom-Net. This research was made possible thanks to the facilities of the TekLiCell platform funded by the Région Rhône-Alpes (ERDF: European regional development fund). LGP2 and 3SR are parts of the LabEx Tec 21 (Investissements d'Avenir—Grant Agreement No. ANR-11-LABX-0030) and of the Energies du Futur and PolyNat Carnot Institutes.

References

Alava M, Niskanen K (2006) The physics of paper. Rep Prog Phys 69:669–723

Alexander SD, Marton R (1968) Effect of beating and wet pressing on fiber and sheet properties. Tappi 51(6): 283–288

Batchelor WJ, He J (2005) A new method for determining the relative bonded area. Tappi J 4(6):23–28

Batchelor WJ, He J, Sampson WW (2006) Inter-fibre contacts in random fibrous materials: experimental verification of theoretical dependence on porosity and fibre width. J Mater Sci 41:8377–8381

Batchelor WJ, Kibblewhite RP, He J (2008) A new method for measuring RBA applied to the page equation for the tensile strength of paper. Appita J 61(4):302–306

Bloch J-F, Rolland du Roscoat S (2009) Three-dimensional structural analysis. In: 14th fundamental research symposium, Oxford, pp 599–664

Eichhorn SJ, Sampson WW (2005) Statistical geometry of pores and statistics of porous nanofibrous assemblies. J R Soc Interface 2:309–318

Fischer WJ, Hirn U, Bauer W, Schennach R (2012) Testing of individual fiber–fiber joints under biaxial load and simultaneous analysis of deformation. Nord Pulp Pap Res J 27(2):237244

Guiraud O, Orgéas L, Dumont PJJ, du Rolland Roscoat S (2012) Microstructure and deformation micro-mechanisms of concentrated fiber bundle suspensions: an analysis

combining X-ray microtomography and pull-out tests. J Rheol 56(3):593–623
He J, Batchelor WJ, Johnston RE (2003) The behavior of fibers in wet pressing. Tappi J 2(12):27–31
Ingmanson WL, Thode EF (1959) Factors contributing to the strength of a sheet of paper. Tappi J 42(1):83–93
Kappel L, Hirn U, Bauer W, Schennach R (2009) A novel method for the determination of bonded area of individual fibre–fibre bonds. Nord Pulp Pap Res J 24:199–205
Kappel L, Hirn U, Gilli E, Bauer W, Schennach R (2010a) Revisiting polarized light microscopy for fiber-fiber bond area measurement—part I: theoretical fundamentals. Nord Pulp Pap Res J 25:65–70
Kappel L, Hirn U, Gilli E, Bauer W, Schennach R (2010b) Revisiting polarized light microscopy for fiber–fiber bond area measurement—part II: proving the applicability. Nord Pulp Pap Res J 25:71–75
Latil P, Orgéas L, Geindreau C, Dumont PJJ, du Rolland Roscoat S (2011) Towards the 3D in situ characterisation of deformation micro-mechanisms within a compressed bundle of fibres. Compos Sci Technol 71:480–488
Le Corre S, Dumont P, Orgéas L, Favier D (2005) Rheology of highly concentrated planar fiber suspensions. J Rheol 49:1029–1058
Leskelä M (1998) Optical properties. In: Paper Physics. Papermaking science and technology, book 16. Paper physics. Fapet Oy, Helsinki, pp 116–137
Luner P, Kärnä AEU, Donofrio CP (1961) Studies in interfibre bonding of paper. The use of optical bonded area with high yield pulps. Tappi J 44(6):409–414
Marulier C, Dumont PJJ, Orgéas L, Caillerie D, du Rolland Roscoat S (2012) Towards 3D analysis of pulp fibre networks at the fibre and bond levels. Nord Pulp Paper Res J 28(2):245–255
Naito T (2002) Struture and structural anisotropy. In: Mark Richard E, Habeger Charles C Jr, Borch Jens, Bruce Lyne M (eds) Handbook of physical testing of paper, revised and expanded, vol 1, 2nd edn. Marcel Dekker, New York, pp 901–1012
Niskanen K, Rajatora H (2002) Statistical geomety of paper cross-sections. J Pulp Pap Sci 28(7):228–233
Niskanen K, Krenlampi P (1998) In-plane tensile properties, chap 5. In: Papermaking science and technology, paper physics, book 16. Fapet Oy, Helsinki
Orgéas L, Dumont PJJ, Vassal J-P, Guiraud O, Michaud V, Favier D (2012) In-plane conduction of polymer composite plates reinforced with architectured networks of copper fibres. J Mater Sci 47:2932–2942
Paavilainen L (1994) Bonding potential of softwood sulphate fibres. Paperi ja Puu 76(3):162–173
Page DH, Tydeman PA, Hunt M (1962) A study of fibre-to-fibre bonding by direct observation, In: 2nd fundamental research symposium on formation and structure of paper, Oxford, pp 171–193
Rolland du Roscoat S, Decain M, Thibault X, Geindreau G, Bloch J-F (2007) Estimation of microstructural properties from synchrotron X-ray microtomography and determination of the REV in paper materials. Acta Mater 55: 2841–2850
Salmén L, Fellers C (1989) The nature of volume hygroexpansivity of paper. J Pulp Paper Sci 15(2):63–65
Sampson W (2004) A model for fibre contact in planar random fibre networks. J Mater Sci 39:2775–2781
Sampson WW (2009a) Materials properties of paper as influenced by its fibrous architecture. Int Mater Rev 54:134–156
Sampson WW (2009b) Modelling stochastic fibrous materials with Mathematica. Springer, London
Schmied FJ, Teichert C, Kappel L, Hirn U, Schennach R (2012) Joint strength measurements of individual fiber-fiber bonds: an atomic force microscopy based method. Rev Sci Instrum 83:073902. doi:10.1063/1.4731010
Schmied FJ, Teichert C, Kappel L, Hirn U, Bauer W, Schennach R (2013) What holds paper together: nanometre scale exploration of bonding between paper fibres. Sci Rep 3:2432. doi:10.1038/srep02432
Seth RS, Jang HF, Chan BK, Wu CB (2003) Transverse dimensions of wood pulp fibres and their implications for end use. In: Baker CF (ed) 11th fundamental research symposium on the fundamentals of papermaking materials, Cambridge, 1997 (trans.). FRC, Manchester, pp 473–503. ISBN: 0-9545272-1-6
Silvy J (1980) Structural study of fiber networks: the cellulosic fiber case. Thèse de docteur d'état. Univ. Grenoble
Thomson CI, Lowe RM, Ragauskas AJ (2007) Imaging celulose fibre interfaces with fluorescence microscopy and resonance energy transfer. Carbohyd Polym 69:799–804
Thomson CI, Lowe RM, Ragauskas AJ (2008a) First characterization of the development of bleached kratf softwood pulp fiber interfaces during drying and rewetting using FRET technology. Holzforschung 62:383–388
Thomson CI, Lowe R, Page D, Ragauskas A (2008b) Exploring fibre-fibre interfaces via FRET and fluorescence microscopy. J Pulp Pap Sci 34:113–119
Toll S (1993) Note: on the tube model for fiber suspensions. J Rheol 37:123–125
Toll S (1998) Packing mechanics of fiber reinforcements. Polym Eng Sci 38:1337–1387
Torgnysdotter A, Kulachenko A, Gradin P, Wågberg L (2007) The link between the fiber contact zone and the physical properties of paper: a way to control paper properties. J Compos Mater 41:1619–1633
Uesaka T, Moss C, Nanri Y (1991) The characterization ofhygroexpansivity in paper. In: Proceedings of the international paper physics conference, vol 1134. TAPPI Press, Atlanta, pp 613–622
Vassal J-P, Orgéas L, Auriault JL, Le Corre S (2008) Upscaling the diffusion equations in particulate media made by highly conductive particles. Part II: application to the fibrous materials. Phys Rev 77:011303
Viguié J, Latil P, Orgéas L, Dumont PJJ, du Rolland Roscoat S, Bloch J-F, Marulier C, Guiraud O (2013) Finding fibres and their contacts within 3D images of disordered fibrous media. Compos Sci Technol 89:202–210
Yang CF, Eusufzai ARK, Sankar R, Mark RE, Perkins RW (1978) Measurements of geometric parameters of fibre networks: part 1. Bonded surfaces, aspect ratios, fibre moments of inertia, bonding site probabilities. Sven Papperstidn 81(13):426–433